Sb_2S_3/AlGaAs based reconfigurable metasurface for dynamic polarization and directionality control of quantum emitter emission: Supporting Information

1. Simulation Setup for Effective Index and Period Calculation

The fundamental operation of the quantum emitter (QE) integrated circular nano-ridge array-based metasurfaces used in our work depends on the efficient coupling of surface plasmon polariton (SPP) to Ag/ SiO_2 interface and their subsequent scattering by the nano-ridge gratings. So, we have conducted 2d FDTD simulations to ensure non-radiative surface waves can be coupled for all possible combinations of the top layer (air, Sb_2S_3, AlAs, or $Al_{0.7}Ga_{0.3}As$) at the desired wavelength (802nm). Based on these calculations, we have selected the heights of Ag and SiO_2 layers as 200nm and 50nm, respectively, for all the PMS structures. The final results and the corresponding planar stacks have been shown in Fig. S1. For these results, the top layer thickness used was 150nm. This value has been used for PMS-2 and 3. However, for PMS-1, the corresponding ridge (top layer) height was 140nm. We have verified that stacks with 140nm top layer also produce SPPs as per requirement (not shown here).

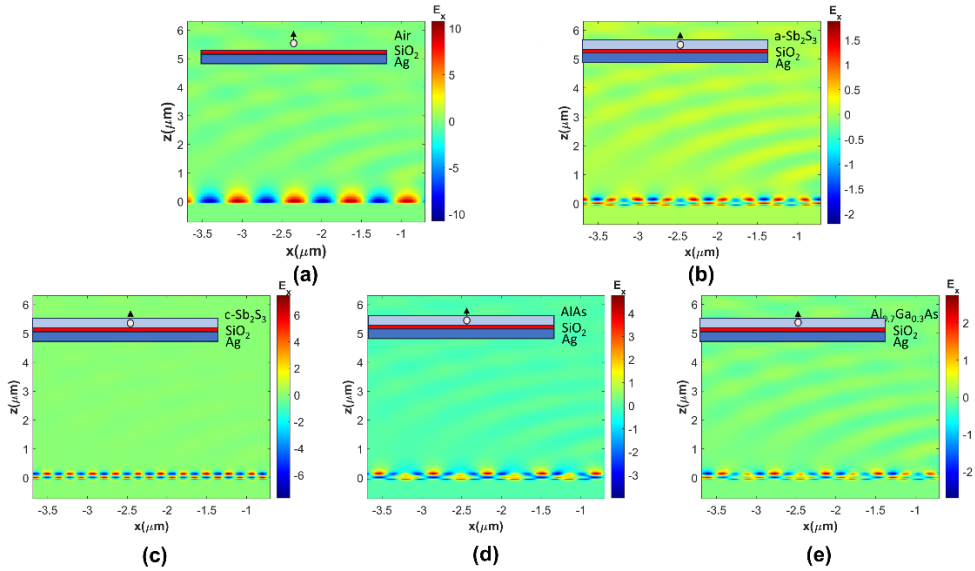

Fig. S1. Surface Plasmon Polaritons (SPP) propagating along the Ag/SiO_2 interface for **(a)** Ag-SiO_2-Air, **(b)** Ag-SiO_2-amorphous Sb_2S_3, **(c)** Ag-SiO_2-crystalline Sb_2S_3, **(d)** Ag-SiO_2-AlAs, **(e)** Ag-SiO_2-$Al_{0.7}Ga_{0.3}As$ stack. The SPP propagation is represented by the electric field component (E_x) along the Ag/ SiO_2 interface. All the electric field values have been normalized by the electric field magnitude of the dipole source. The specific structures are shown in the insets of respective figures. The surface waves are excited by a dipole source of wavelength 802nm placed 50nm above the SiO_2 top surface in the simulation environment. For all the simulations, the heights of Ag, SiO_2, and the top layer (Sb_2S_3, AlAs, or $Al_{0.7}Ga_{0.3}As$) have been kept constant at 200nm, 50nm, and 150nm respectively.

To ensure effective scattering of the surface waves, the period (P) of the bullseye grating needs to be carefully selected. This value is calculated using the equation [1]

$$P = \frac{\lambda_0}{N_{eff}} \tag{S1}$$

where, λ_0 is the free-space propagating wavelength of the outgoing photons, which has been matched to the QE emission wavelength for high directional beams [2]. The SPP effective mode index (N_{eff}) is calculated using the effective medium theory.

For PMS-1, each circular ridge in the array is composed of AlAs and Sb_2S_3 (Fig. 2(a), (b) of the main text) with a height of 140nm. Using the same setup as in the insets of Fig. S1(a), (b), and (d) with the top layer height of 140nm, we calculated the effective indices to be N_1 =1.127, N_2=2.398, and N_4=2.463 respectively. Considering the fill-factors for AlAs and Sb_2S_3 to be both 0.2, the value of N_{eff} becomes 1.648 ($= 0.6N_1 + 0.2N_2 + 0.2N_4$), translating into P of 486.65nm as per Eq. S1. Repeating the same calculations for crystalline-Sb_2S_3 gives P=458nm. Since PMS-1 will switch between amorphous and crystalline states of Sb_2S_3, we have chosen P to be 475nm for this structure. For PMS-2, the calculation was done with a fill-factor of 0.35 for AlGaAs and 0.05 for Sb_2S_3. For PMS-3, the fill factor values considered are 0.5 and 0.1, respectively.

We have also shown the spectral intensity response for different QE wavelengths for all three structures in Fig. S2. We would like to clarify that the QE considered in all the other simulations in this work has a single emission wavelength (802nm). But to verify the calculations of P, we have varied the emission wavelength for this particular set of simulations. Our goal in choosing P using Eq S1 is to match the peak scattered light intensity with the emission wavelength of NE8 centers (802nm). This ensures a high degree of directionality of the emitted photons. All the structures were simulated using the 2d simulation setup shown in Fig. S2(g). The structural parameters for all three structures are the same as the ones used for calculating P (using Eq. S1), as stated in the previous paragraph.

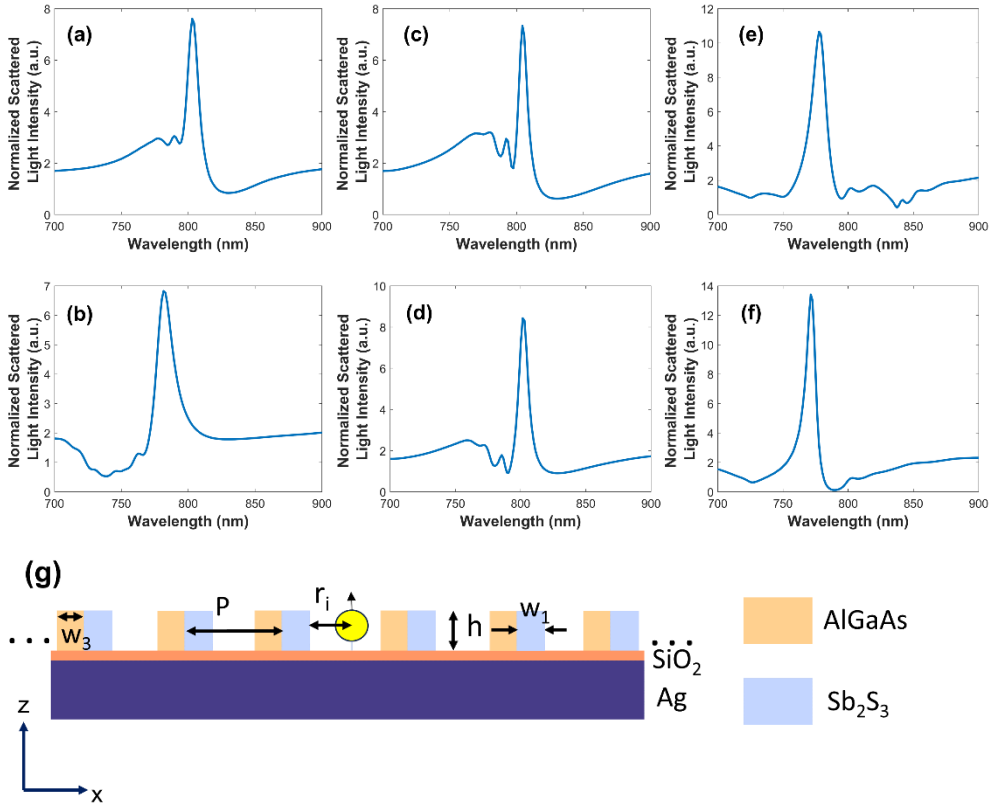

Fig. S2. Scattered light intensity spectra for **(a)-(b)** PMS-1, **(c)-(d)** PMS-2, and **(e)-(f)** PMS-3 for different QE wavelengths with crystalline and amorphous Sb_2S_3, respectively. **(g)** 2d

Simulation setup used for the simulations. The structural parameters used are the ones for which the period was calculated using Eq. S1. For example, for PMS-1 P=475nm, w_1=0.2*P (Fill factor 0.2), and w_3=0.2*P (Fill factor 0.2), h=140nm, and r_i=515nm. All the intensity values have been normalized by the QE intensity.

The results show that for both PMS-1 and PMS-2, the peak intensity of scattered light occurs roughly at 802nm for the design parameters for both states of Sb_2S_3. However, for PMS-3, the intensity of the scattered light is relatively low at the 802nm wavelength for both states. This is maybe caused by the choice of inner radius for this structure. Our simulations show as we increase r_i from 515nm keeping the other parameters constant, the intensity peak moves towards 802nm and almost perfectly coincides with 802nm for r_i=615nm (not shown here). However, for r_i=615nm, the phase requirements cannot be matched properly. This mismatch in the peak intensity position with NE8 emission wavelength (802nm) even for the optimized parameters may be one of the reasons why the final PMS-3 architecture has a slightly lower Purcell Factor (PF) compared to other structures. This postulate regarding the low PF of PMS-3 is based on the idea that the normalized scattering intensity has quite similar profile to that of the PF of the 2d structure. So, we can safely assume that the 3d structure PF will have a similar misalignment leading to a low PF at 802nm. Having said that, this phenomenon of low PF of PMS-3 definitely requires further investigation to pinpoint the physical mechanism dictating it.

2. Calculation of Stokes Parameters

The Stokes parameters (S_0, S_1, S_2, S_3) are calculated using the following set of equations [3]

$$S_0 = |E_x|^2 + \left|E_y\right|^2 \tag{S2}$$

$$S_1 = |E_x|^2 - \left|E_y\right|^2 \tag{S3}$$

$$S_2 = 2|E_x||E_y|\cos(\psi_y - \psi_x) \tag{S4}$$

$$S_3 = 2|E_x||E_y|\sin(\psi_y - \psi_x) \tag{S5}$$

where, $|E_{x(y)}|$ and $\psi_{x(y)}$ represent the magnitude and phase of the x(y) component of scattered electric field respectively. The normalized Stokes parameter (P_C) is calculated using the following equation

$$P_C = \frac{S_3'}{\sqrt{S_1'^2 + S_2'^2 + S_3'^2}} \tag{S6}$$

where, S_1', S_2', and S_3' are obtained by normalizing the corresponding Stokes parameter by the total intensity (S_0).

The numerator (S_3') in Eq. S6 represents the difference in intensity between right and left circular polarized states at a given point. The denominator measures the total polarized light intensity. So, P_C can be used to define extent and chirality of circular polarization. The values -1, 0, and +1 represent pure left circular, linear and right circular polarizations respectively.

3. Optical Parameters of Different Materials

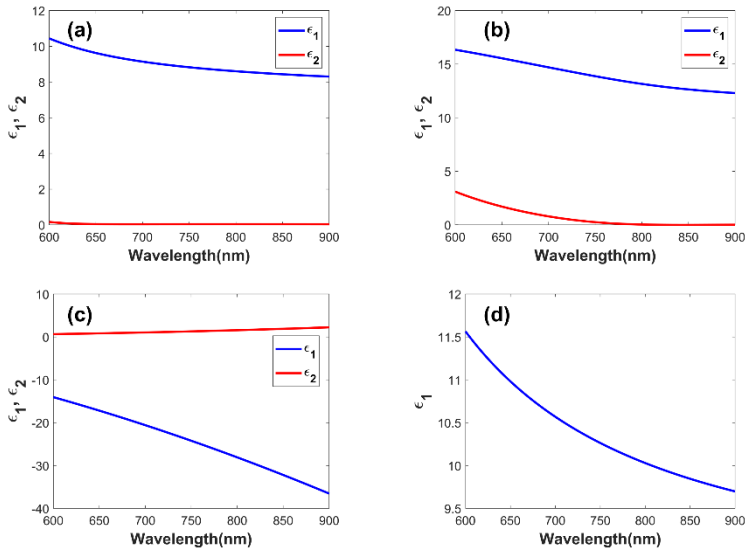

Fig. S3. Optical parameters of different materials used in the FDTD simulations. Real (ε_1) and imaginary (ε_2) parts of relative permittivity of **(a)** amorphous Sb_2S_3, **(b)** crystalline Sb_2S_3 [4], and **(c)** Silver [5]. **(d)** Real part of relative permittivity of $Al_{0.7}Ga_{0.3}As$ [6]. The imaginary part of relative permittivity of $Al_{0.7}Ga_{0.3}As$ is quite small and has been considered to be zero in our simulations. The refractive index of AlAs has been considered constant at 3 in our simulations [7].

4. Choosing the Mole Fraction *x* of $Al_xGa_{1-x}As$ for Different PMS Structures

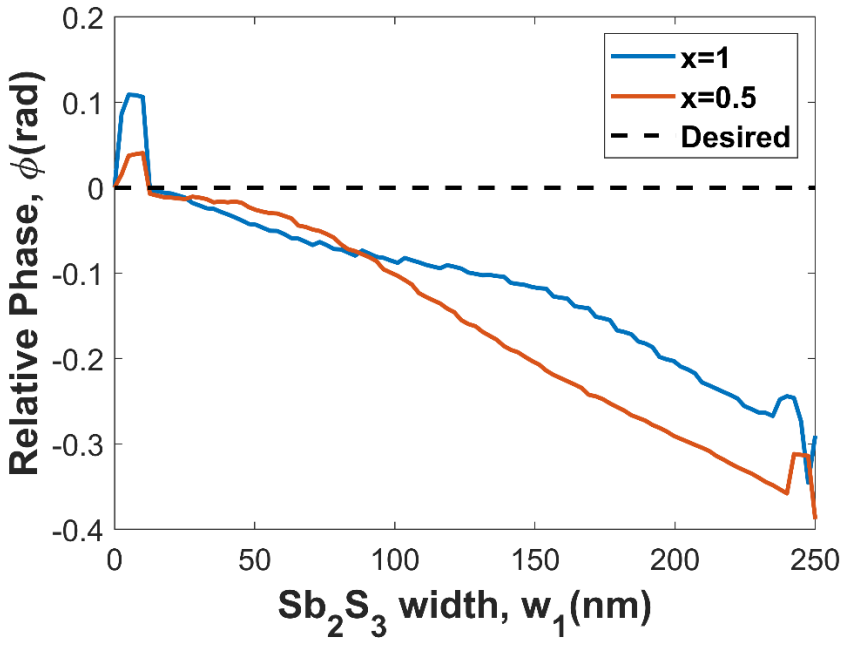

Fig. S4. Realized and required relative phase values of the scattered light for different Sb_2S_3 layer widths (w_1) for x=0.5 and 1 for the AA state of PMS-1. For both simulations, the total ridge width (w_2) has been maintained at 250nm, with the same 2d simulation setup shown in Fig. 3(a) of the main text. AlAs has a refractive index very close to amorphous Sb_2S_3, which ensures a small relative azimuthal phase shift of the scattered light in the amorphous phase as the width of Sb_2S_3 increases in expense of AlAs layer, a requirement for producing RP scattered light in the AA state. Changing the mole fraction x to 0.5 produces a larger phase shift, as expected. Based on the results, we have chosen AlAs (x=1) as the second material of the ridge in the PMS-1R and PMS-1L structures.

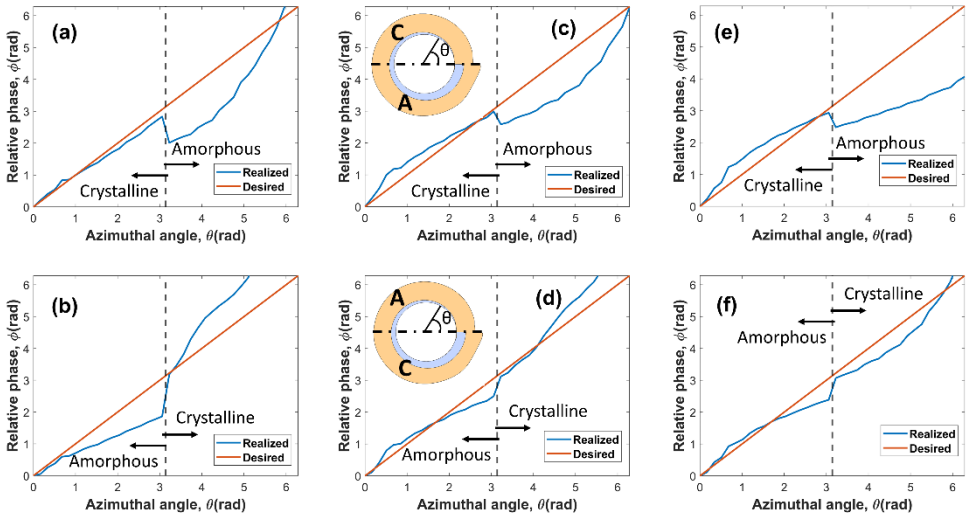

Fig. S5. Realized and required relative phase values of the scattered light at different azimuthal positions (θ) for **(a)-(b)** x=0.5, **(c)-(d)** x=0.7, and **(e)-(f)** x=1 for the CA and AC states respectively of the PMS-2R structure. Simulations setups used for the phase calculations are the same as the one depicted in Fig. 3(a) of the main text. As can be seen, the phase profiles in both the AC and CA states best match the required value for x=0.7. So, we have used $Al_{0.7}Ga_{0.3}As$ as the second material in the circular ridge of PMS-2R and PMS-2L.

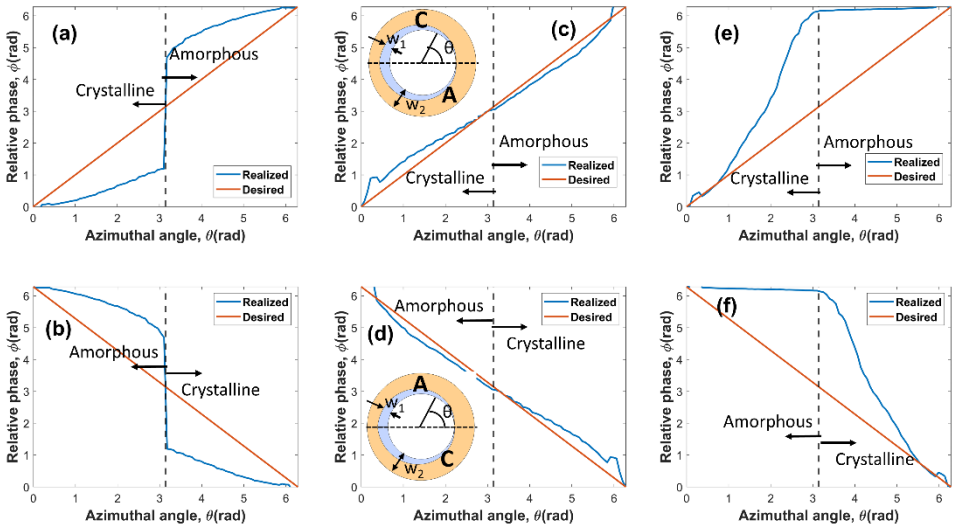

Fig. S6. Realized and required relative phase values of the scattered light at different azimuthal positions (θ) for **(a)-(b)** x=0.5, **(c)-(d)** x=0.7, and **(e)-(f)** x=1 for the CA and AC states respectively of the PMS-3 structure. As can be seen, the phase profiles in both the AC and CA states best match the required value when x=0.7. This is because $Al_{0.7}Ga_{0.3}As$ has a refractive index roughly in between the amorphous and crystalline states of Sb_2S_3. This makes sure that an equal and opposite change of spatial phase profile is achieved for the two states as w_1 increases. Such contrasting spatial phase profiles are necessary for producing opposite spin

states of the scattered light in the two states of PMS-3, as explained in the main text. So, we have used $Al_{0.7}Ga_{0.3}As$ as the second material in the circular ridge. Simulations setups used for the phase calculations are the same as the one depicted in Fig. 3(a) of the main text.

5. Scattering Properties of Amorphous and Crystalline Sb_2S_3 Blocks

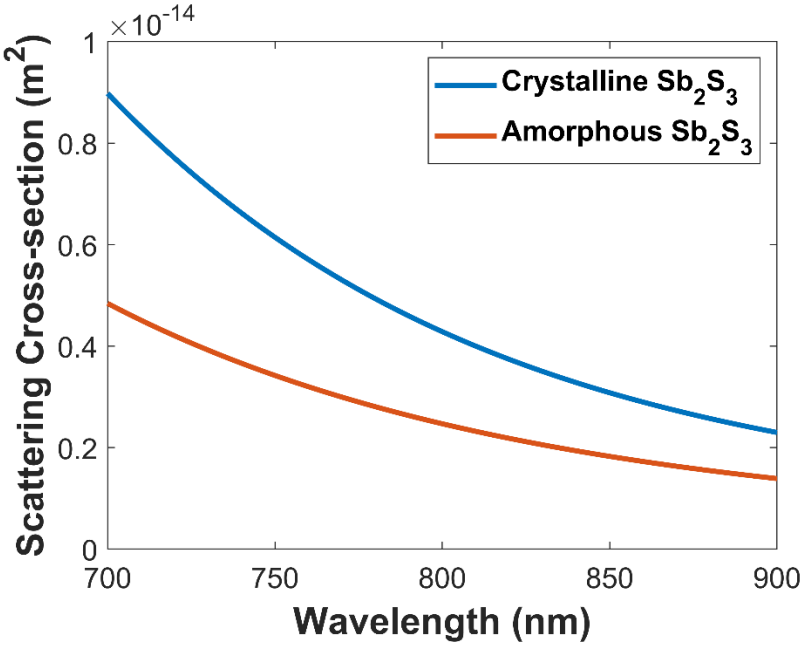

Fig. S7. Scattering cross-section spectra of a Sb_2S_3 nano-cube with dimensions 150nm in the crystalline and amorphous states. The higher refractive index in the crystalline state means it has a higher scattering cross-section. The fact that such nano-cubes are the building blocks of the scattering ridges in the metasurfaces, this result further validates our observation that higher refractive index crystalline Sb_2S_3 produces higher scattering in PMS-2 (Fig. 6) and PMS-3 (Fig. 9).

6. Co-ordinates used for the far-field patterns

Lumerical FDTD Solutions projects any far-field pattern onto an imaginary hemispherical surface. To represent it on a flat piece of paper, the coordinates (u_x, u_y) were used for the plots in the main text. This can be compared to looking straight down the imaginary hemisphere, with (u_x, u_y)=(0,0) representing scattering along the normal direction in our case.

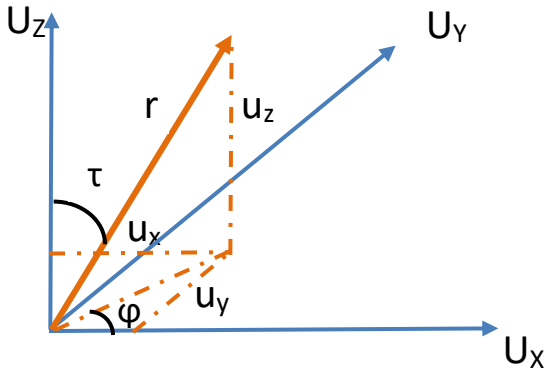

Fig. S8. Relation between spherical coordinate and (u_x, u_y, u_z) co-ordinate system used in this work.

Eq. S7-S10 show the mathematical relationship between the well-known spherical coordinate system (r, φ, τ) and the (u_x, u_y, u_z) coordinate system used in this work. The exact definitions of variables like τ and φ with respect to u_x, u_y, and u_z can be found in Fig. S8.

$$u_x = \sin(\tau)\cos(\varphi) \tag{S7}$$

$$u_y = \sin(\tau)\sin(\varphi) \tag{S8}$$

$$u_z = \cos(\tau) \tag{S9}$$

$$u_z = \sqrt{1 - u_x^2 - u_y^2} \tag{S10}$$

References

1. S. K. Andersen, S. Bogdanov, O. Makarova, et al., "Hybrid plasmonic bullseye antennas for efficient photon collection," Acs Photonics 5, 692–698 (2018).
2. Y. Kan, S. K. Andersen, F. Ding, et al., "Metasurface-enabled generation of circularly polarized single photons," Adv. Mater. 32, 1907832 (2020).
3. E. Collett, "Field guide to polarization," (Spie Bellingham, WA, 2005).
4. M. Delaney, I. Zeimpekis, D. Lawson, D. W. Hewak and O. L.Muskens, Advanced Functional Materials, 2020, 30, 2002447.
5. E. D. Palik, Handbook of optical constants of solids, Academic press, 1998, vol. 3.
6. D. Aspnes, S. Kelso, R. Logan and R. Bhat, Journal of applied physics, 1986, 60, 754–767.
7. R. Fern and A. Onton, Journal of applied physics, 1971, 42, 3499–3500